Journal of Geodesy (2024) 98:110
https://doi.org/10.1007/s00190-024-01918-2

ORIGINAL ARTICLE

Estimating three-dimensional displacements with InSAR: the strapdown approach

Wietske S. Brouwer[1] · **Ramon F Hanssen**[1]

Received: 8 September 2023 / Accepted: 30 October 2024

Abstract
Deformation phenomena on Earth are inherently three dimensional. With SAR interferometry (InSAR), in many practical situations the maximum number of observations is two (ascending and descending), resulting in an infinite number of possible displacement estimates. Here we propose a practical solution to this underdeterminancy problem in the form of the strapdown approach. With the strapdown approach, it is possible to obtain "3D-global/2D-local" solutions, by using minimal and largely undisputed contextual information, on the expected driving mechanisms and/or spatial geometry. It is a generic method that defines a local reference system with transversal, longitudinal, and normal (TLN) axes, with displacement occurring in the transversal-normal plane only. Since the orientation of the local frame is based on the physics of the problem at hand, the strapdown approach gives physically more relevant estimates compared to conventional approaches. Moreover, using an a-priori uncertainty approximation on the orientation of the local frame it is possible to assess the precision of the final estimates. As a result, appropriate cartographic visualization using a vector map with confidence ellipses enables an improved interpretation of the results.

Keywords InSAR · Geodesy · Surface displacements · Decomposition · Strapdown

1 Introduction

InSAR scatterers obtained from SAR interferometry are typically not situated at ideal locations, and the observations have an imaging geometry that is not optimal for retrieving full three-dimensional (3D) displacements. Moreover, they are only sensitive to the projection of the 3D displacement vector onto the radar line-of-sight (LoS) direction, d_{LoS}, along a plane orthogonal to the LoS (Massonnet and Feigl 1998; Fialko et al. 2002; Hanssen 2001; Wright et al. 2004b; Brouwer and Hanssen 2023), i.e.,

$$\begin{aligned} d_{\mathrm{LoS}} &= P_{\mathrm{LoS}^{\perp}}\, d_{\mathrm{ENU}}, \\ &= [\sin\theta \sin\alpha_d, \sin\theta \cos\alpha_d, \cos\theta]\, d_{\mathrm{ENU}}, \end{aligned} \tag{1}$$

where $d_{\mathrm{ENU}} = [d_e, d_n, d_u]^T$ is the 3D displacement vector in east, north, and up direction, respectively.[1] $P_{\mathrm{LoS}^{\perp}}$ is the orthogonal projector onto the LoS, where θ is the incidence angle toward the radar, and α_d is the azimuth of its zero-Doppler plane (ZDP) at the position of the target, in the direction toward the satellite, see Brouwer and Hanssen (2023, Fig. 1).

A decomposition of the LoS displacement vector into three orthogonal directions would be ideal. Yet, this requires at least three independent LoS observations from significantly different viewing geometries, but since almost all the SAR satellites operate right-looking,[2] orbiting the Earth in near-polar retrograde orbit, they have very similar viewing geometries and the maximum number of available and effective observations often reduces to two, i.e., ascending and descending, resulting in an underdetermined problem with an

✉ Wietske S. Brouwer
w.s.brouwer@tudelft.nl

Ramon F Hanssen
r.f.hanssen@tudelft.nl

[1] Delft University of Technology, Stevinweg 1, 2628, CN, Delft, The Netherlands

[1] Note that a displacement vector d, with unit [mm], may also be interpreted as, e.g., an (average or instantaneous) displacement velocity, unit [mm/y], since this is geometry-invariant.

[2] Adding an observation from a left-looking radar will improve the accuracy for the estimated parameters (Rocca et al. 2003; Wright et al. 2004a), but the precision for the estimated north component is still rather poor.

Published online: 30 November 2024

infinite number of solutions along a solution line (Brouwer and Hanssen 2023).

Contemporary InSAR information products come in two classes: the geodetic products, which use mainly geometric information and minimal or no information on the physics, and the geophysical products, which aim at producing best-fit models describing the physical mechanisms at hand. Many geodetic InSAR information products, including most publicly available ones, circumvent the problem of underdetermination by disregarding the north component of the deformation, and asserting a decomposition into the east and up components only (Crosetto et al. 2020). Yet, it is well known that this approach produces inherently biased estimates, particularly for the up component (Brouwer and Hanssen 2023). An alternative geodetic option is using the the null-line aligned (NLA) coordinate system as proposed by Brouwer and Hanssen (2023), which ensures unbiased estimates, but produces results that can be more challenging to interpret for non-experts. For geophysical products, there is a wide range of more optimal models, including the possibility to use the LoS observations directly in for instance modeling of fault slip or magma reservoir pressure change. Since these types of inversions can work directly with LoS data, no decomposition is required.[3]

Here we demonstrate a practical, effective, and largely generic solution to the problem of underdetermination, introducing the 'strapdown' method, which uses a location-dependent local reference system that is tuned to the deformation phenomenon.

Special cases of this approach have been applied in particular applications, such as landslides (Mohr 1997; Colesanti and Wasowski 2006; Notti et al. 2014; Cascini et al. 2010; Greif and Vlcko 2012; Van Natijne et al. 2022), ice sheets (Joughin et al. 1998; Mattar et al. 1998; Mohr et al. 1998; Ford et al. 2003), and line-infrastructure (Chang et al. 2018; Özer et al. 2019). Yet, apart from being a wider generalization and a mathematical framework, the strapdown approach offers complete error propagation and therefore a proper quality description of the final estimated displacements. Moreover, effectively it leads to an optimal unbiased solution which is locally two dimensional, but globally three dimensional, requiring only a limited degree of rather undisputed contextual information on the expected deformation phenomena.

We first discuss the geometry of the strapdown approach and the deformation phenomena for which it can be used in Sect. 2. In Sect. 3, we discuss how the displacements can be estimated and we elaborate on the quality of the estimated displacements. Finally, we demonstrate the strapdown approach in two examples in Sect. 4 and reflect on the method in Sect. 6.

2 System geometry

In the following, we define the geometry of the strapdown system and elaborated on different classes of deformation phenomena.

2.1 The local strapdown coordinate system

Instead of choosing one coordinate system for the entire area of interest, we define a local, right-handed Cartesian coordinate system that is fixed to the local deformation phenomenon with transversal, longitudinal, and normal (TLN) components, $d_{\mathrm{TLN}} = [d_T, d_L, d_N]^T$, see Fig. 1.

The term *local* implies that the orientation of the TLN frame will differ for each location, hence the term '*strapdown*', adapted from inertial navigation technology (Titterton et al. 2004). Thus, a displacement vector d_{TLN} is projected onto the LoS with Eq. (1) as Chang et al. (2018):

$$d_{\mathrm{LoS}} = P_{\mathrm{LoS}^\perp} R_1 R_2 R_3 d_{\mathrm{TLN}} = P^R_{\mathrm{LoS}^\perp} d_{\mathrm{TLN}}, \tag{2}$$

where R_1, R_2, and R_3 are rotation matrices:

$$R_1 = \begin{bmatrix} \cos\Lambda & \sin\Lambda & 0 \\ -\sin\Lambda & \cos\Lambda & 0 \\ 0 & 0 & 1 \end{bmatrix}, \tag{3}$$

$$R_2 = \begin{bmatrix} 1 & 0 & 0 \\ 0 & \cos\Phi & -\sin\Phi \\ 0 & \sin\Phi & \cos\Phi \end{bmatrix}, \tag{4}$$

$$R_3 = \begin{bmatrix} \cos\Omega & 0 & \sin\Omega \\ 0 & 1 & 0 \\ -\sin\Omega & 0 & \cos\Omega \end{bmatrix}, \tag{5}$$

where $\Lambda \in [0°, 360°)$ is the azimuth of the longitudinal direction (L) relative to the north.[4] The elevation angle of the longitudinal direction is $\Phi \in (-90°, +90°]$, relative to the horizontal (where up-hill is positive) and the elevation angle of the transversal direction (T) is $\Omega \in (0°, +90°]$. The normal direction (N) completes the orthogonal right-handed TLN system. $P^R_{\mathrm{LoS}^\perp}$ is the projector that projects the displacement vector d_{TLN} onto the LoS along a plane orthogonal to

[3] In this study, we focus on interferometric estimates of displacements. In case of large displacements, SAR offset tracking may provide an additional displacement observable (Gray et al. 1998; Scheiber and Moreira 2000; Strozzi et al. 2002; Bechor and Zebker 2006).

[4] Due to the 180° ambiguity in longitudinal direction, in case of a topographic slope or a subsidence slope, the longitudinal axis is defined tangential to the local iso-elevation or isodeformation lines, such that the positive transversal direction is always directed downslope. In the absence of a clear slope, we use the smallest angle w.r.t. the north, i.e., $\Lambda \in (-90°, +90°]$, following (Chang et al. 2018).

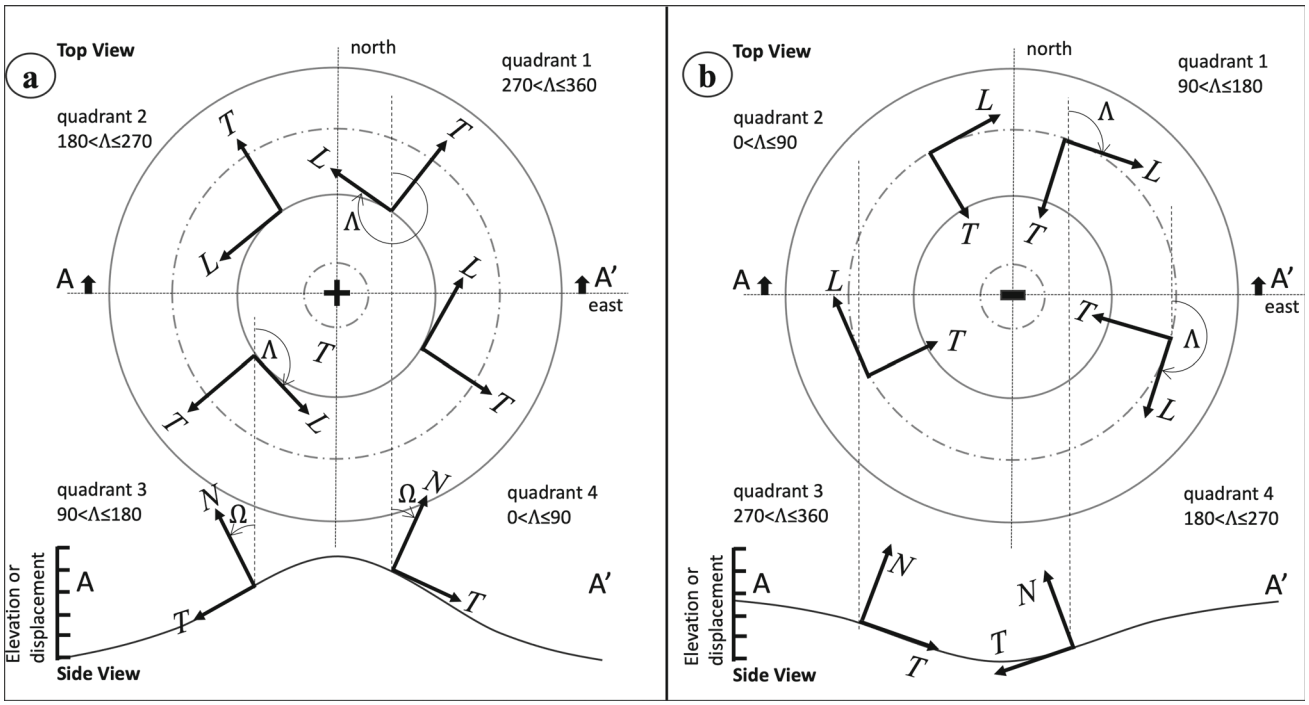

Fig. 1 Orientation of the TLN reference system for gravity-induced downslope deformation phenomena and/or subsidence and uplift. **a** shows the orientation for a schematized mountain (with iso-elevation lines) or equivalently an uplift dome (with iso-displacement lines). Note that the transversal direction is always downslope or centrifugal. Therefore, the slope aspect determines the boundaries within which Λ should lie. **b** Similar situation sketch for a valley or equivalently a subsidence bowl. Note that the transversal axis is always downslope, and thus centripetal for subsidence

the LoS. Thus, $P^R_{\mathrm{LoS}^\perp}$ is a function of Λ, Ω, and Φ with size 1×3, i.e., $P^R_{\mathrm{LoS}^\perp} = [P_T, P_L, P_N]$, see App. A.

Geometrically, any displacement vector can be regarded as being situated in a 2D plane, with zero-displacement in the complementary direction, by definition. In the TLN frame, the displacement vector is always situated in the plane spanned by the transversal and normal unit vectors, and is therefore by definition zero in the longitudinal direction. Note that this is not an assumption or an approximation, as it follows deductively from the definition of the coordinate system. Of all 2D planes that contain the displacement vector as subset, there is typically only one plane orientation that is physically genuinely relevant, i.e., uniquely interpretable. This is due to the fact that all observable displacements are caused by forces, or stresses, that are acting upon the object. In many cases, displacement mechanisms of interest have a physical context that can be regarded as 'known' to some extent. Obviously, the force of gravity is omnipresent in every case, and is in many cases also the root cause of the observed motion. In other cases, forces are due to kinetic causes, such as deforming roads and railways imposed by traffic load or due to, e.g., volumetric (e.g., a subsidence bowl caused by a subsurface volume change) or tectonic mechanisms (Yu et al. 2013; Cavalié and Jónsson 2014). Consequently, we can orient the TLN system, viz. the longitudinal direction, to the direction in which there is physically no displacement to be expected, as we will elaborate below. From orthogonality, the longitudinal direction defines the local *displacement plane*, in which the two orthogonal displacement components (T and N) are situated. With this definition, Eq. (2) can be locally solved with LoS observations from two sufficiently different viewing geometries. Consequently, the main challenge is (i) to find the orientation of the local displacement plane in 3D space, given by (Λ, Φ, Ω) and (ii) to approximate the precision of these orientation parameters in order to perform an error propagation to assess the final quality of the local solution.

2.2 Deformation phenomena

The generic description of the methodology can be elaborated for typical classes of deformation phenomena. Here we discuss downslope displacements, subsidence and uplift, (line)-infrastructure, and motion associated with idealized faults. Note that when the displacement direction can be considered as 'known' (e.g., vertical), the LoS observations can be projected directly on the unit vector of the displacement direction, and the strapdown system is not necessary.

2.2.1 Gravity-driven downslope deformation

Landslides, moving glaciers, or slope instabilities of a dike are examples of phenomena where the main deformation occurs in a vertical plane that contains the downslope direction and the local gravity vector. The plane is perpendicular to the local gradient and gravity is the main driving force, see Fig. 1.

When the longitudinal axis is parallel to the iso-elevation lines of the slope of the occurring landslide, it can, in first approximation, be assumed that the forces in the longitudinal direction will be negligible, i.e., $d_L = 0$. Hence, all displacements are expected to occur in the (vertical) plane spanned by the transversal and normal axis, shown in the side views of Fig. 1, and $\Phi = 0°$ by definition, see Eq. (5). The slope *aspect*, α_a, i.e., the compass direction that a terrain surface faces, determines the value for the angle Λ since the (angle of the) slope, Ω, is always referred to as a positive number, see Fig. 1, i.e., $\alpha_a = \Lambda + 90°$. The positive transversal direction is always directed downslope.

Note that these approximations are a strong simplification of reality. In certain cases, displacements along the longitudinal axis can occur, e.g., in a glacier where the gravitational force may induce internal stresses, which may result in displacements along the longitudinal direction.

2.2.2 Subsidence and uplift

Subsidence bowls and uplift domes are caused by a subsurface volume change, in combination with gravity, see Fig. 1, e.g., as a result of fluid pressure decrease or increase (Geertsma 1973; Dzurisin and Lisowski 2007) or due to surface loading or unloading. These types of phenomena exhibit vertical and horizontal displacement components (Kratzsch 1983). The horizontal displacement directions are in first approximation centripetal for subsidence, and centrifugal for uplift (Müller and Preusse 2018). The longitudinal direction, indicated by azimuth Λ, is oriented parallel to the isodeformation lines, and the transversal direction is downslope (centripetal) for subsidence, and centrifugal for uplift. Similar to the downslope case, there is—by definition—no displacement component in the longitudinal direction. The normal displacements are maximum in the center of the field, decreasing asymptotically to the edge of the field. The example in Sect. 4.1 elaborates this further.

2.2.3 Line-infrastructure

Line-infrastructure assets are characterized by an extended spatial dimension in one direction (by definition the longitudinal direction), where the spatial extent in the other two directions is limited, such as roads, railways, dikes, and pipelines. The slope of the asset is given by Φ, while Ω represents the cant of the asset or the slope in the transversal direction (Chang et al. 2014, 2018). The latter is usually small, see Fig. 2. Often, it is possible to assume that no significant continuous (stationary) displacements occur in the longitudinal direction (Chang et al. 2014, 2018; Özer et al. 2019), apart from perhaps thermal expansion and contraction which can be independently modeled and has a non-secular character.

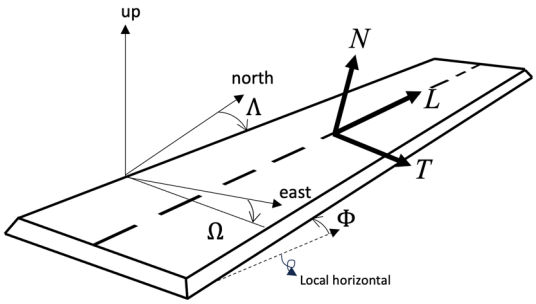

Fig. 2 The orientation of the TLN reference system for line-infrastructure: Λ and Φ represent the azimuth and slope of the longitudinal direction, respectfully, and Ω the cant. Figure adapted from Chang et al. (2014)

2.2.4 Motion associated with faults

Although deformations resulting from tectonics (post, co-, and inter-seismic) may often be too complex to uniquely identify the 2D plane in which the displacements occur, we can still utilize the strapdown method for first-order approximations and deformations associated with faults as hydrological boundaries. Considering, e.g., rising mine water after mine closure associated with normal or reverse faults (Caro Cuenca et al. 2013), see Fig. 3. In such cases the driver of the deformation is sufficiently well defined and determines its directionality. As a result, no displacements are expected along the fault and the longitudinal direction can thus be directed parallel to the fault. In Sect. 4.2, this example is further elaborated. For ideal strike-slip faults, the sides move along each other and the longitudinal direction is directed perpendicular to the fault. To prevent directional ambiguity, the smallest azimuth angle is chosen, i.e., $\Lambda \in (-90°, 90°]$. For all three fundamental fault types, d_T has a different sign at both sides of the fault.

Obviously, there will be many cases in which slip on a fault will not enable a simple unambiguous directionality assumption for the displacement, in which cases more advanced (geophysical) models are required.

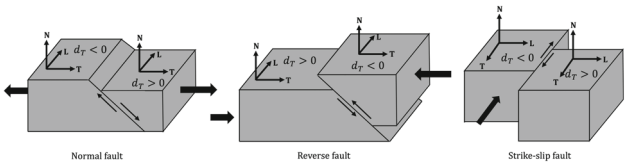

Fig. 3 Orientation of the TLN reference frame for the fundamental types of fault motion (Fowler 1990). For normal and reverse faults, displacement is expected to occur dominantly in a vertical plane perpendicular to the strike of the fault, which aligns with the longitudinal direction. For vertical strike-slip faults, horizontal displacement happens dominantly parallel to the strike direction, and the longitudinal direction is thus aligned perpendicular to the strike of the fault

3 Estimating displacements using the strapdown approach

As longitudinal displacements are null by definition, any displacement vector can be unambiguously represented in a 2D (d_T, d_N) system, and thus d_T and d_N can be estimated with two LoS observations. There are several options for estimating d_T and d_N. Chang et al. (2014, 2018) add a pseudo-observation, $d_L = 0$, to the mathematical model. However, this approach requires the orientation of the TLN frame to be perfectly known, since a misalignment will result in biased estimates for d_T and d_N. Adding pseudo-observation $d_L = 0$ to the system of equations, while in fact $d_L \neq 0$, results in a 'decomposition error' similar to 'neglecting' the north component in a conventional ENU decomposition, see Brouwer and Hanssen (2023). In reality, the orientation of the TN-plane will always have some alignment uncertainty, expressed by σ^2_{Λ}, σ^2_{Ω}, and σ^2_{Φ}. A better alignment precision results in a better estimation of the unknown displacements d_T and d_N. Below, we consider the impact of the alignment uncertainty in the mathematical model.

3.1 The mathematical model

Since the longitudinal displacements are null by definition, d_L can be removed from Eq. (2) and $P^R_{\text{LoS}^\perp}$ reduces to a 1×2 matrix with only P_T and P_N, see App. A, and the 2×1 displacement vector contains only d_T and d_N. The TLN frame orientation is introduced using pseudo-observations $\underline{\Lambda}$, $\underline{\Omega}$, and $\underline{\Phi}$ (the underline indicates the stochastic nature of the observable) in the mathematical model:

$$E\{\underbrace{\begin{bmatrix} \underline{d}^{(1)}_{\text{LoS}} \\ \vdots \\ \underline{d}^{(m)}_{\text{LoS}} \\ \underline{\Lambda} \\ \underline{\Omega} \\ \underline{\Phi} \end{bmatrix}}_{y}\} = \underbrace{\begin{bmatrix} a_1(x) \\ \vdots \\ a_m(x) \\ a_{m+1}(x) \\ a_{m+2}(x) \\ a_{m+3}(x) \end{bmatrix}}_{A(x)}, \text{ and} \tag{6}$$

$$D\{\underbrace{\begin{bmatrix} \underline{d}^{(1)}_{\text{LoS}} \\ \vdots \\ \underline{d}^{(m)}_{\text{LoS}} \\ \underline{\Lambda} \\ \underline{\Omega} \\ \underline{\Phi} \end{bmatrix}}_{y}\} = \underbrace{\begin{bmatrix} Q_{\text{LoS},1} & \cdots & 0 & 0 & 0 & 0 \\ \vdots & \ddots & \vdots & 0 & 0 & 0 \\ 0 & \cdots & Q_{\text{LoS},m} & 0 & 0 & 0 \\ 0 & 0 & 0 & \sigma^2_{\Lambda} & 0 & 0 \\ 0 & 0 & 0 & 0 & \sigma^2_{\Omega} & 0 \\ 0 & 0 & 0 & 0 & 0 & \sigma^2_{\Phi} \end{bmatrix}}_{Q_{yy}}, \tag{7}$$

where for $i \in [1, m]$

$$\begin{aligned} a_i(x) &= P^{(i)}_T(\Lambda, \Omega, \Phi)d_T + P^{(i)}_N(\Lambda, \Omega, \Phi)d_N \\ a_{m+1}(x) &= \Lambda \\ a_{m+2}(x) &= \Omega \\ a_{m+3}(x) &= \Phi, \end{aligned} \tag{8}$$

and $x = [d_T, d_N, \Lambda, \Omega, \Phi]^T$ is the vector of unknown displacements and orientation angles. $E\{.\}$ expresses the expectation of the model, which can be solved with at least two sets, i.e., $m = 2$, of LoS observations: $\underline{d}^{(1)}_{\text{LoS}}$ and $\underline{d}^{(2)}_{\text{LoS}}$, each having a different viewing geometry. Here, a 'set' refers to all observations from one particular viewing geometry, either ascending or descending, over a region of uniform motion (RUM).[5] Note that the size of each set can be different due to a different number of LoS observations, which can be either point scatterers (PS) or distributed scatterers (DS). Rows $i \in [1, m]$ in matrix A are nonlinear equations of x, where each row is unique due to the difference in viewing geometry. To overcome the rank deficiency, pseudo-observations for $\underline{\Lambda}$, $\underline{\Omega}$, and $\underline{\Phi}$ are added representing our best-effort approximation for the frame orientation. These values can be purely data-driven based on iso-displacement lines retrieved from the original line-of-sight results, or on contextual information, as long as conservative precision estimates are used. $D\{.\}$ is the dispersion of the model, where

[5] For a successful estimation of x, the two LoS observations 'sets' need to be spatio-temporally coinciding and independent (STCI). As this is hardly ever possible, a region of uniform motion (RUM) needs to be defined and a datum connection (in time and space) needs to be performed. Moreover, the two LoS observation sets need to have a sufficient angular diversity. For in-depth elaboration see Brouwer and Hanssen (2023).

$Q_{\text{LoS},i}$ is the covariance matrix of the LoS observations for set i. This covariance matrix is a diagonal matrix containing the variances of displacements for each PS or DS within the set. The off-diagonal elements are null, since all PS or DS within a set represent different physical scatterers. The uncertainty in our best-effort attempt to orient the TLN frame, or equivalently the level of trust that we have in our knowledge in the orientation of the frame, is represented in σ^2_{Λ}, σ^2_{Ω}, and σ^2_{Φ}. Choosing these values realistically (we recommend conservatively) is important, as this uncertainty propagates into the (co)variances of the final displacement parameters, which is a key feature of the strapdown methodology.

3.1.1 Parameter estimation

To estimate the five unknown parameters and provide a proper quality description the linearized system of equations needs to be solved,

$$\Delta \underline{y}_{[0]} \approx J_{[0]} \Delta x_{[0]}, \tag{9}$$

where

$$J_{[0]} = \begin{bmatrix} \frac{\partial}{\partial d_T} a_1(x_{[0]}) & \dots & \frac{\partial}{\partial \Phi} a_1(x_{[0]}) \\ \vdots & \vdots & \vdots \\ \frac{\partial}{\partial d_T} a_{m+3}(x_{[0]}) & \dots & \frac{\partial}{\partial \Phi} a_{m+3}(x_{[0]}) \end{bmatrix} \tag{10}$$

is the Jacobian matrix which is a function of the initial approximations for the unknown parameters $x_{[0]}$, i.e.,

$$x_{[0]} = \left[d_{T_{[0]}}, d_{N_{[0]}}, \Lambda_{[0]}, \Omega_{[0]}, \Phi_{[0]} \right]^T, \tag{11}$$

which yield initial approximations for the observation vector $\underline{y}$ and $\Delta \underline{y}_{[0]} = \underline{y} - A(x_{[0]})$. Consequently, when $m \geq 2$, Δx can be estimated using

$$\Delta \hat{\underline{x}}_{[0]} = \begin{cases} J^{-1}_{[0]} \Delta \underline{y}_{[0]}, & \text{for } m = 2, \text{ and} \\ Q_{\hat{x}\hat{x}} J^T_{[0]} Q^{-1}_{yy} \Delta \underline{y}_{[0]} & \text{for } m > 2, \end{cases} \tag{12}$$

$$Q_{\hat{x}\hat{x}} = \begin{cases} J^{-1}_{[0]} Q^{-1}_{yy} J^{-1}_{[0]}, & \text{for } m = 2, \text{ and} \\ \left(J^T_{[0]} Q^{-1}_{yy} J_{[0]} \right)^{-1} & \text{for } m > 2, \end{cases} \tag{13}$$

where $Q_{\hat{x}\hat{x}}$ represents the precision of x. The new estimate for $\hat{\underline{x}}$ is defined as $\hat{\underline{x}}_{[1]} = x_{[0]} + \Delta \hat{\underline{x}}_{[0]}$, and can be used to estimate $\Delta x_{[1]}$. Iteration leads to a final estimate for $\hat{\underline{x}}$. An estimation of the unknown parameters requires rough initial approximations for which either prior knowledge of the deformation phenomenon can be used, or initial assessments from the original LoS estimates. For $\Lambda_{[0]}$, $\Omega_{[0]}$, and $\Phi_{[0]}$ the best-effort frame orientations are used.

The precision of the five estimated parameters is expressed by the (co)variances in $Q_{\hat{x}\hat{x}}$, sketched for an arbitrary frame orientation in Fig. 4.

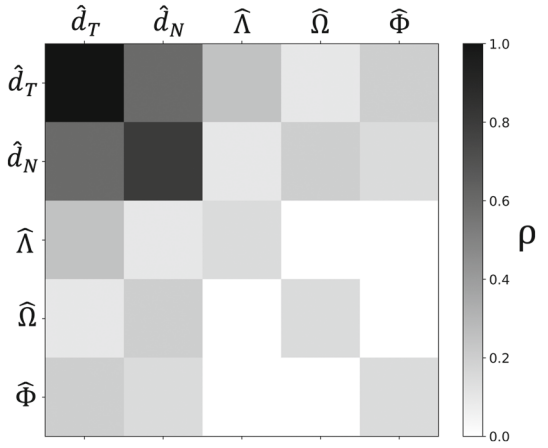

Fig. 4 Sketch of (normalized) $Q_{\hat{x}\hat{x}}$ for an arbitrary frame orientation. The diagonal elements represent the precision of the estimated parameters $\hat{x}$ and the off-diagonal terms the correlation between them. There is correlation between the estimated displacements (upper-left 2×2 block) but no correlation between the estimated frame orientation (lower-right 3×3 block). However, there is correlation between the estimated frame orientations and the estimated displacements (e.g., lower-left 3×2 block)

In this example, there is correlation between $\hat{\underline{d}}_T$ and $\hat{\underline{d}}_N$, in the upper 2×2 block. Due to the choice of the pseudo-observations, there is no correlation between the estimated orientation angles $\hat{\underline{\Lambda}}$, $\hat{\underline{\Omega}}$, and $\hat{\underline{\Phi}}$, i.e., $\rho = 0$. Yet, there is correlation between the displacements and the angular estimates. Different frame orientations will result in different levels of correlation.

3.2 The quality of the estimates

The precision of the estimates $(\hat{\underline{d}}_T, \hat{\underline{d}}_N)$ depends on four independent contributions: (i) the actual (true) orientation of the TLN frame, (ii) the actual (true) magnitude of the d_T and d_N displacements, (iii) the alignment precision of the TLN frame, and (iv) the precision of the observations and pseudo-observations. These will be discussed below.

3.2.1 True orientation of the TLN frame

The actual (true) orientation of the TLN frame has a dominant impact on the precision of the final estimates. With two LoS observation geometries (ascending and descending), displacement components in the direction of the *null-line* (Brouwer and Hanssen 2023) cannot be observed: the more either the transversal or normal direction aligns with the null-line, the less precise that parameter can be estimated. The most favorable option is therefore when the plane spanned by the transversal and normal axis (TN-plane) is orthogonal to the null-line, i.e., when $\Lambda = \phi$ and $\Phi = \zeta$, where ϕ and

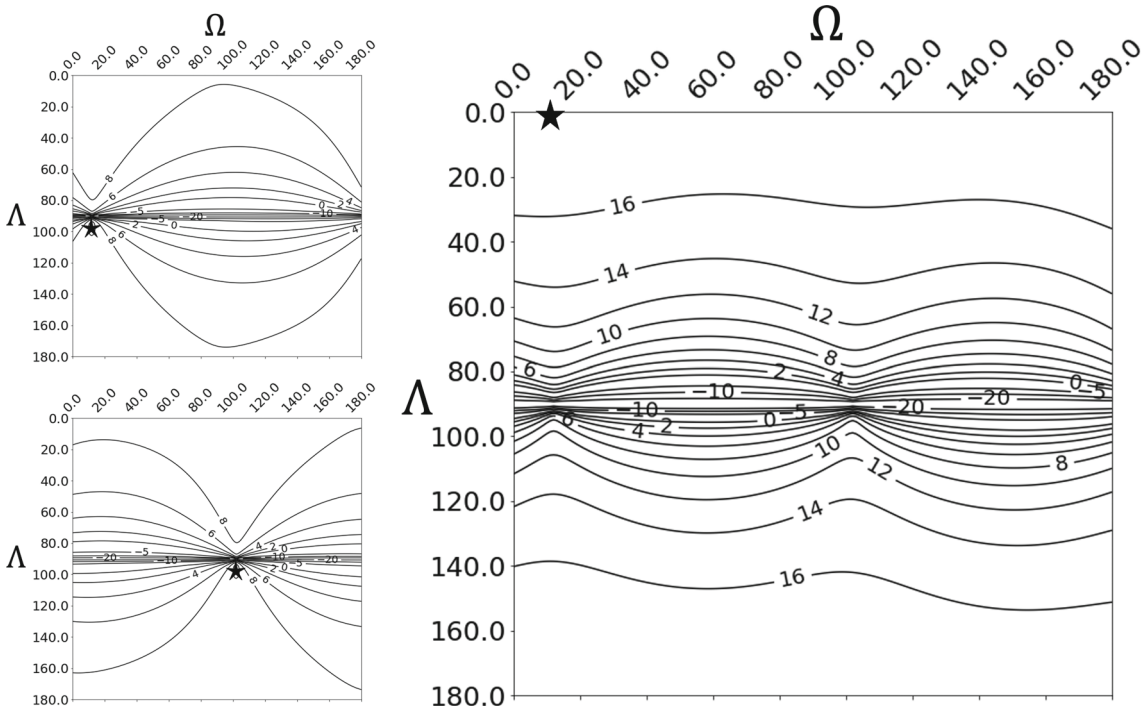

Fig. 5 SNR [dB] for the normal (upper-left) and transversal (lower-left) component for different orientations of the TLN frame. The observation geometry of the simulated ascending and descending acquisition is presented in Table 1, which result in a null-line orientation, $n(\phi, \zeta) = n(0.14°, 12.14°)$. The right figure shows the sum of the left two figures since one is always interested in estimating both components. It can be seen that the SNR of the two combined directions is greatest when the longitudinal direction is in the direction of the null-line, indicated by the black star. In that specific case, the TN-plane is orthogonal to the null-line

Table 1 Simulated viewing geometries and consequent null-line orientation

Geometry	Inc. angle θ	Azim. ZDP α_d
Ascending	32°	250°
Descending	40°	105°
Null-line n	$\phi = 0.14°$	$\zeta = 12.14°$

ζ are the azimuth angle and elevation angle of the null-line, respectively.[6]

Figure 5 shows the signal-to-noise ratio (SNR) for the transversal (lower-left) and normal (upper-left) component as a function of Λ and Ω, with $\Phi = 0°$. We simulate an arbitrary displacement phenomenon with $d_T = d_N$, observed from an ascending and a descending orbit with viewing characteristics as presented in Table 1.

For different frame orientations, we simulate LoS observations and subsequently estimate the unknown parameters x with Eq. (12). In Fig. 5, we show the SNR for each realization, where $\text{SNR}_T = 10\log_{10}(d_T/\sigma_{d_T})$, and $\text{SNR}_N = 10\log_{10}(d_N/\sigma_{d_N})$ represent the transversal and normal direction, respectively, shown by the two left figures. The quality of the estimated normal component is best when the transversal direction aligns with the null-line, shown by the black star in Fig. 5. Likewise, the quality for d_t is the best when the normal direction aligns with the null-line. Obviously, when one of the two components aligns with the null-line, both satellite geometries have zero sensitivity in that direction, and both observations are entirely attributed to the other component.

In reality, we need to estimate *both* components in concert. Therefore we show the sum of the SNR ratios in the right figure, i.e., $\text{SNR}_{\text{total}} = \text{SNR}_N + \text{SNR}_T$. The black star shows the most favorable orientation with the highest SNR value, which occurs when the longitudinal direction is aligned with the null-line, e.g., $\Lambda = \phi$ and $\Omega = \zeta$. The quality of the estimates is poor when $\Lambda \approx 90°$, i.e., when the normal or transversal direction is in the direction of the null-line.

3.2.2 True magnitude of d_T and d_N

The quality (both bias and precision) of $(\hat{d}_T, \hat{d}_N)$ is scaled by the actual (but unknown) size of the displacement signal. This follows from the Jacobian in Eqs. (10) and (11), which requires initial values for $d_{T_{[0]}}$ and $d_{N_{[0]}}$. The quality of the displacement estimates, i.e., $\sigma_{\hat{d}_T}$ and $\sigma_{\hat{d}_N}$, is thus a function of

[6] In this special case the TLN frame is identical to the nullline aligned (NLA) frame, see Brouwer and Hanssen (2023).

the Jacobian matrix containing the values of d_T and d_N from the second to last iteration step. Therefore, larger estimated displacements lead to a larger uncertainty (or σ values), since $\sigma_{\hat{d}_T}$ and $\sigma_{\hat{d}_N}$ also capture the potential bias due to a misalignment in the frame. In the case of a misalignment, $\sigma_{\hat{d}_T}$ and $\sigma_{\hat{d}_N}$ are biased: larger for larger deformations and smaller for smaller deformations. In the most extreme case, if there is no deformation, there is also no bias.

3.2.3 Alignment precision of the TLN frame

Any error in the best-effort orientation approximation of the TLN frame, i.e., a misalignment, results in $d_L \neq 0$, and consequently biased estimates for d_T and d_N. Misalignments are taken into account in Eqs. (6) and (7), via σ_Λ, σ_Ω, and σ_Φ, propagating the alignment uncertainty to the precision for the final estimates, see Eq. (13). The alignment precision needs to be chosen conservatively, i.e., not too optimistic. As long as the true 'unknown' frame orientation falls within the estimated uncertainty, then the bias obtained on $\hat{\underline{d}}_T$ and $\hat{\underline{d}}_N$ will also fall within the estimated precision defined by $\sigma_{\hat{d}_T}$ and $\sigma_{\hat{d}_N}$. Furthermore, since the frame orientation is both an unknown (as part of x) and a pseudo-observation (as part of y), the final estimated frame orientation is equal to the pseudo-observation, i.e., the initial estimated orientation.

3.2.4 Precision of (pseudo) observations

The fourth contribution to the precision of the estimates $(\hat{\underline{d}}_T, \hat{\underline{d}}_N)$ is the quality (or precision) of (i) the LoS observations and (ii) the pseudo-observations, expressed in Q_{yy} in Eq. (13). Obviously, a higher quality of the observations, and/or more certainty in the frame orientation, results via $Q_{\hat{x}\hat{x}}$ in higher quality of the final estimates.

3.3 Interpretation of the results

For a cartographic uniform visualization of the estimated (d_T, d_N) displacements there are two options. When the orientation of the strapdown coordinate system is uniform over the area of interest, it is possible to create a panchromatic map[7] for d_T and d_N separately, see, e.g., Fig. 11e and f. However, in the more generic case of a spatially variable orientation of the strapdown coordinate system this is not possible anymore, since directionality needs to be considered. A *vector* (quiver) map type is more suitable in this case, see Figs. 6 and 8.

This has the added value that the precision of both magnitude and direction can be expressed using a confidence ellipse. The relative sizes of the vector and the confidence ellipse enable a direct assessment of the significance of the estimate and of the SNR, and hence improve interpretability. In Fig. 6, the estimated transversal displacement vector d_T, located at the geometric center of a RUM, is situated at geographic coordinates (x_i, y_i). In this case the normal direction is practically aligned with the up direction.[8] The error ellipse shows the confidence region, with transversal axis $p\,\sigma_T$, and longitudinal axis $\sigma_L = d_T \tan(p\,\sigma_\Lambda)$ where p expresses the desired size of the confidence region, i.e., for $p = 2$ we have a 95% confidence region. Both σ_T and σ_Λ follow from Eq. (13).

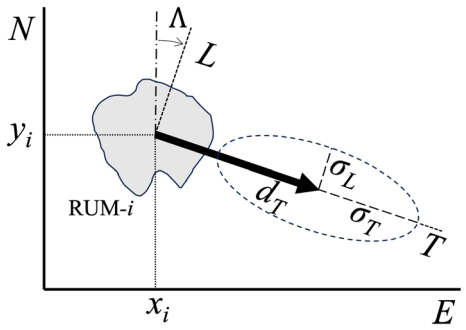

Fig. 6 Vector representation of strapdown results of RUM-i at geographic (east,north) coordinates (x_i, y_i), showing the estimated transversal displacement component, d_T. The error ellipse or confidence region has two axes. The size of transversal axis is σ_T and the size of the longitudinal axis is $\sigma_L = d_T \tan \sigma_\Lambda$

Table 2 Acquisition details for Sentinel-1 tracks 15 and 139 at Veendam, the Netherlands

	S1 track 15	S1 track 139
Heading	Ascending	Descending
Mean θ	36.3°	44.2°
Mean α_d	261°	98°
Start	Aug 7, 2018	Aug 4, 2018
End	Mar 8, 2020	Feb 16, 2020

4 Results: 2 case studies

In this section, we apply the strapdown approach on two case studies: subsidence due to solution mining and displacements resulting from ground water pressure in relation to faults.

4.1 Magnesium extraction in Veendam

In Veendam, the Netherlands, solution mining for multi-component salts occurs at a depth of ∼1500 m. Around the production caverns, salt starts flowing toward the caverns (Brinkman 2016). Subsequently, the overlaying rock

[7] Or similarly a contour map or a dot distribution map.

[8] In other cases, the displacement vector can be situated along the slope.

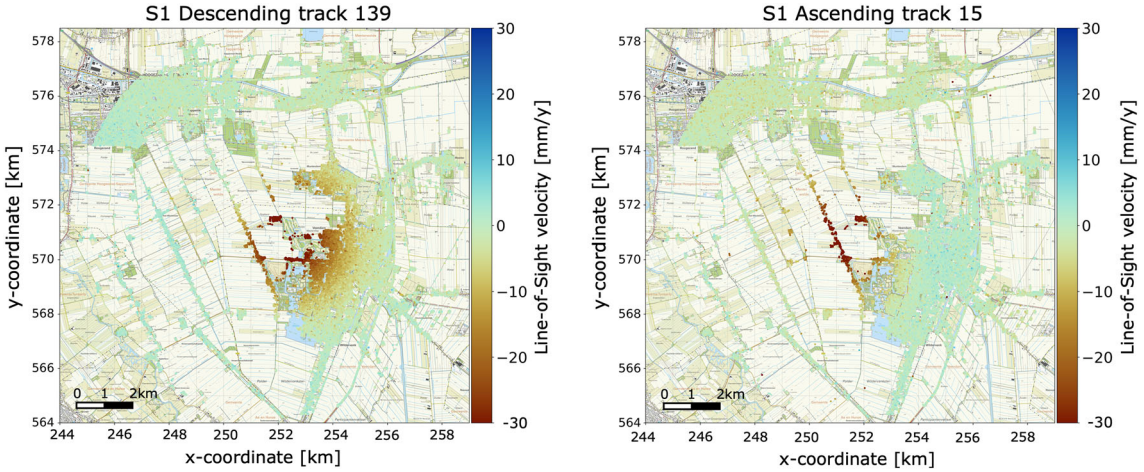

Fig. 7 Estimated LoS velocities for S1 descending track 139 and ascending track 15 for Veendam. The location of the maximum LoS velocity differs for both tracks. This is an early indicator for significant horizontal displacements

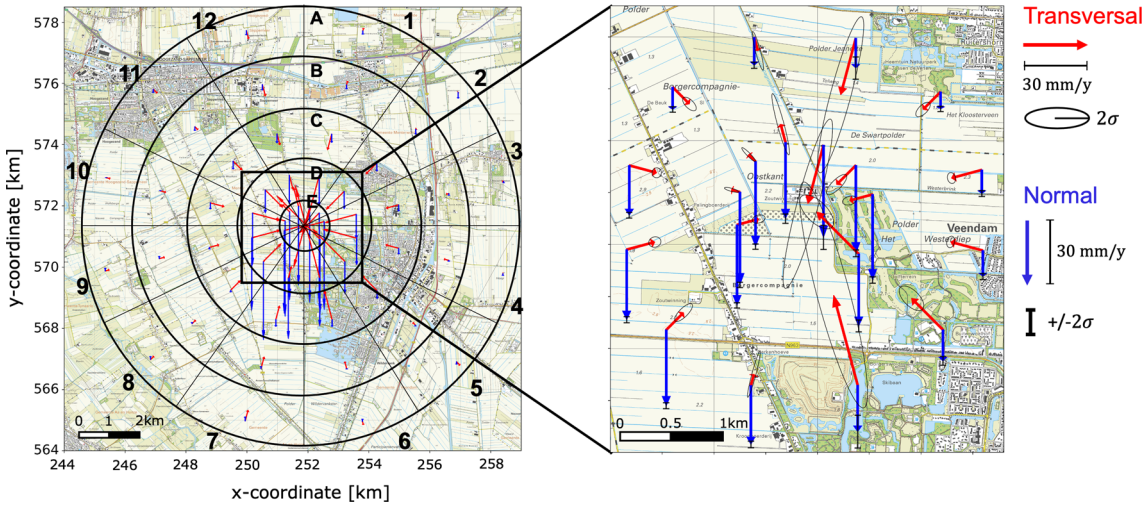

Fig. 8 Results for strapdown approach for a subsidence bowl resulting from magnesium solution mining. Red vectors represent the estimated displacement velocity in the Transversal direction (near-horizontal), and their 2σ uncertainty is visualized by a 95% confidence ellipse. Blue vectors represent the displacement velocities in the Normal direction (near-vertical), which have a $\pm 2\sigma$ confidence interval. The vectors start at the center of gravity for each RUM

layers move downwards and horizontally toward the center of the cavern, resulting in a subsidence bowl. The observed vertical displacements will be greatest at the center of the bowl, while the horizontal displacements are centripetal, see Sect. 2.2.2. We use the strapdown approach to estimate the unknown 3D displacements. The area is monitored by Sentinel-1 from descending and ascending acquisitions, see Table 2, using a PSI approach (van Leijen 2014).

The LoS results for both geometries are shown in Fig. 7. For the descending acquisition, the greatest LoS velocities occur more to the east compared to the ascending acquisition, which is an indicator for significant horizontal displacements. For the strapdown decomposition the ascending and the descending acquisition need to have the same spatial datum, where the velocity is either known or assumed to be equal to zero. In this case the reference points for both geometries are chosen in a presumedly stable area outside the mining activities.

4.1.1 RUM definition

As the orientation of the TLN frame varies within the region, in first iteration we approximate the subsidence bowl assuming radial symmetry and divide it into 12 sectors and five equidistant radial areas, see Fig. 8, where each element is assumed to behave as a region of uniform motion (RUM). To account for imperfect circularity we set $\sigma_\Lambda = 5°$, implying that, with a 95% confidence interval, we conservatively esti-

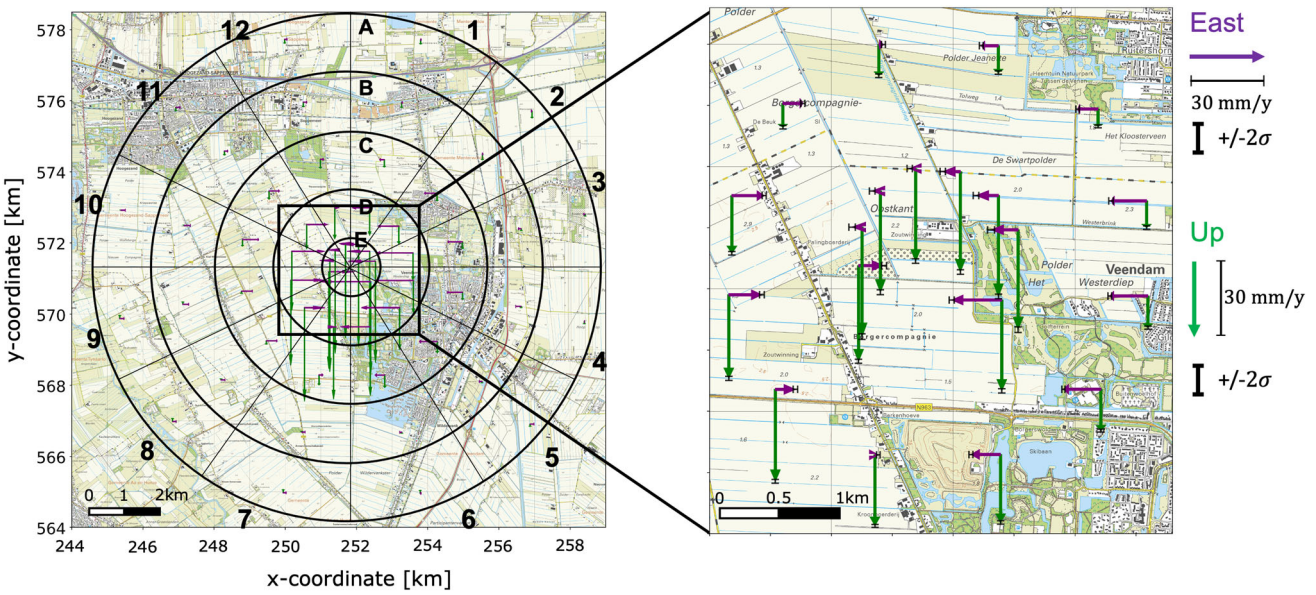

Fig. 9 Conventional (biased) results for comparison, showing only east and up displacements, produced by erroneously ignoring the north component. Note that this is a decomposition error (Brouwer and Hanssen 2023) with a bias mainly in the up component, see Fig. 10

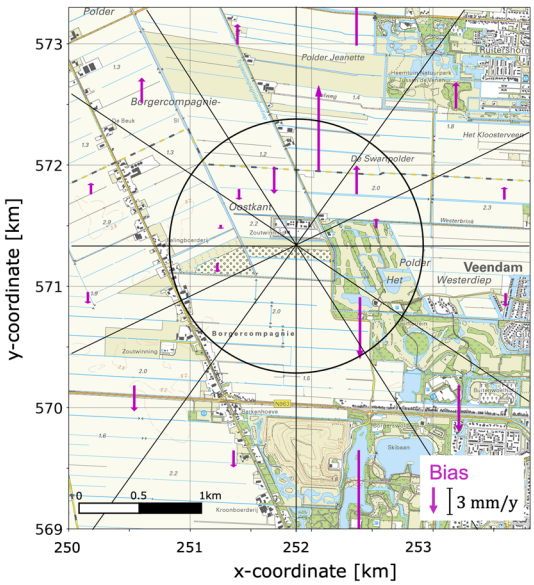

Fig. 10 Bias in the estimated Up components introduced by erroneously using the conventional east-up approach. The vectors show the difference with the estimated Normal components per RUM. Upward and downward point vectors show overestimation and underestimation, respectively

mate the Λ^0 alignment to be within $\pm 10°$. We use $\Omega^0 = 0°$ and $\Phi^0 = 0°$ due to the absence of significant topography, and we set $\sigma_\Omega = 2°$ and $\sigma_\Phi = 2°$, to quantify our confidence in this assumption.

Table 3 Acquisition details Radarsat-2 (Limburg)

	Track 109	Track 302
Heading	Ascending	Descending
Mean θ	37.3°	33.4°
Mean α_d	259.2°	100.9°
Start	Dec 14, 2016	Dec 4, 2016
End	Sep 12, 2020	Sep 26, 2020

4.1.2 Parameter estimation per RUM

Independently for each RUM we estimate the mean LoS displacement velocity for each viewing geometry, i.e., $\hat{v}^{\text{asc}}_{\text{LoS}}$ and $\hat{v}^{\text{dsc}}_{\text{LoS}}$, based on all time-series of the scatterers within that particular RUM. We approximated $\sigma_{v^{\text{asc}}_{\text{LoS}}}$ and $\sigma_{v^{\text{dsc}}_{\text{LoS}}}$ by calculating the RMSE of the LoS velocities of the individual scatterers with the mean velocities, these values are used for $Q_{\text{LoS},i}$ in Eq. (7). Subsequently, we estimate the average velocities in the transversal and normal direction, $\hat{v}_T$ and $\hat{v}_N$, with Eqs. (6) and (7), see Fig. 8. The largest mean normal (near-vertical) displacement of ~40 mm/y indeed occurs at the center of the subsidence bowl. RUMs A4, A6, A7, and A8 contain only scatterers in one viewing geometry, impeding strapdown estimates.

We estimate the precision for the unknown velocities, $Q_{\hat{x}\hat{x}}$, visualized by 2σ confidence ellipses and error bars for the normal velocities. The minor axes of the ellipses represent the level of confidence due to the uncertainty in the alignment of the frame. The uncertainty of both the transversal and the normal velocity differs per RUM. Since the orientation of

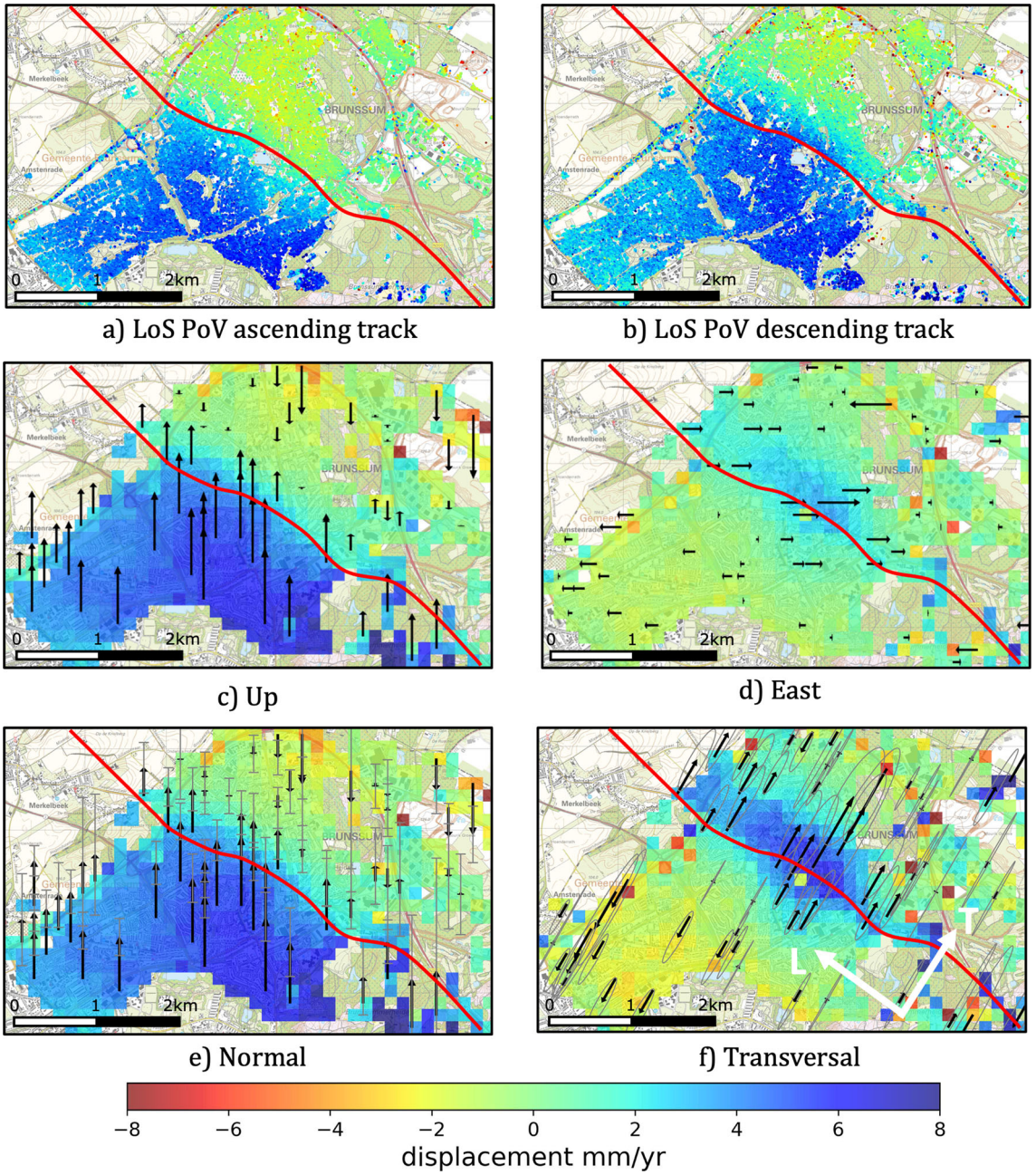

Fig. 11 Estimated displacement rates (mm/y) for the area of Brunssum, the Netherlands. The Feldbiss fault runs trough the middle of the city in the direction NW-SE, indicated by the red line. **a** and **b**: LoS displacement rates projected onto the vertical (PoV) for the ascending and descending track, respectively. **c** and **d**: vertical and east displacement rates, by neglecting the north component. Note that this is decomposition error that typically results in biased estimates (Brouwer and Hanssen 2023). Blue values in **d** indicates eastbound motion. **e** and **f**: normal and transversal displacement rates estimated with the strapdown approach. Blue values in **e** indicate a positive motion in the normal direction, which is upward. Blue and orange values in **f** indicate displacements in the positive and negative transversal direction, respectively. In **c**–**f** we plotted displacement vectors, and for strapdown approach also confidence regions. These vectors are only plotted for a subset of randomly selected RUMs, in order to keep the visualization interpretable

the null-line is near-north ($\phi = 0.7°$ and $\zeta = 7.1°$), the transversal direction is almost in the direction of the null-line for RUMs 1, 12, 6, and 7, which is properly addressed by the confidence regions for these regions. It can be seen that also the normal component is affected.

For comparison, the conventional biased approach is followed where the north component is neglected and only the east and up components are estimated, leading to a decomposition error (Brouwer and Hanssen 2023). In Fig. 9, we show the biased estimated east and up components using that approach. The comparison shows that the strapdown approach captures the entire 3D deformation phenomenon: while we estimate 2D displacements per RUM, we retrieve the full 3D displacement phenomenon by combining all RUMs, hence the *'2D-local, 3D-global'* characterization.

In Fig. 10, we show the difference in estimated velocity between the up component from the east-up approach and the normal component in the strapdown approach. As expected, the greatest errors, up to −5.4 mm/y, occur in RUMs located in the north and south (e.g., 12, 1, 6, and 7), due to the large neglected north component. It also proves that the conventional approach results in biased estimates: for a subsidence bowl it is highly unlikely that—for some reason—there will be zero displacements into the north direction. As a result, in the conventional decomposition the neglected north component is attributed to the estimated up component, and depending on the sign of the north component, the up component is over- or underestimated. Therefore, we expect to see (i) larger differences between the up and normal components for the RUMs in the north and south and (ii) a changing sign for the difference since the true north displacements for these RUMs also have a different sign.

In comparison, the neglect-north approach results in (i) no information on the north component at all (even if it would be significant enough to be estimated reliably), and (ii) less accurate (i.e., biased) estimates in the east and north components. The strapdown approach leads to three-dimensional unbiased (east-north-up) estimates, accompanied with realistic precision metrics that enable realistic interpretation.

4.2 Hydrological effects in relation to faults

From 1900 until 1970, coal was extracted from mines in Limburg, the Netherlands (Van Bergen et al. 2007). One of its after-effects is differential ground heave induced by rising mine water (Pöttgens 1985; Caro Cuenca et al. 2013). Three major ground heave zones are known, one of which is situated near Brunssum along the NW-SE oriented Feldbiss fault (Heitfeld and Klunker 2016; Van Balen et al. 2021). Here we investigate the displacements near this fault over a relatively short period of four years.

4.2.1 Deformation phenomenon and RUMs

The Brunssum area is monitored by Radarsat-2 from an ascending and a descending geometry, see Table 3. Differential displacements are estimated using a PSI approach, for both geometries independently (van Leijen 2014). The LoS displacement rate estimates are projected onto the vertical (PoV) with $d_{\mathrm{PoV}} = \cos^{-1}\theta d_{\mathrm{LoS}}$, see Fig. 11a and b. Close to the Feldbiss fault, the two acquisition geometries clearly show different results, which is an indication for significant horizontal displacement components.

For comparison, we estimate the conventional up ('vertical') and east velocities, by neglecting the north-bound displacement components, resulting in biased estimates, see Brouwer and Hanssen (2023). The resulting vertical and east displacement rates are presented in Fig. 11c and d, respectively. They suggest that the area is moving upward at the southwest side of the fault, while at the northeast side, the vertical displacements seem minimal. The estimated east displacement rates, Fig. 11d, are difficult to interpret, since they underestimate the real horizontal displacement rates.

From the LoS displacement estimates we hypothesize that the surface movement is correlated with the orientation of the Feldbiss fault, and that the horizontal displacements are directed orthogonal to it, as the driving mechanism is most likely related to the redistribution of subsurface water pressure. There is no physical indication to assume a strike-slip component (parallel to the fault direction) in this case. Therefore, we use the strapdown approach where for each RUM the longitudinal axis is defined parallel to the Feldbiss fault. Since the orientation of the TLN frame is the same for the entire area, we divide the area into grid cells of 150×150 m.

4.2.2 Parameter estimation per RUM

Per grid cell (RUM), we estimate the mean LoS displacement rate, and the RMSE which serves as a quality estimate for Q_{LoS} in Eq. (7) for both the ascending and descending acquisition, assuming a common datum, and we compute the mean incidence angle and azimuth of the ZDP. Subsequently, we estimate the normal and transversal displacement rates using Eqs. (6) and (7) and estimate the frame orientation parameters to be $\Lambda_{[0]} = -55°$ and $\Omega_{[0]} = \Phi_{[0]} = 0°$, using $\sigma_\Lambda = 20°$ and $\sigma_\Omega = \sigma_\Phi = 5°$ for each grid cell.

The estimated transversal and normal displacement rates per grid cell are shown in Fig. 11e and f. For a random subset of grid cells we also added the estimated displacements as vectors including an error bar and 95% confidence ellipse for the normal and transversal component, respectively. At the southwest, we find positive displacements in the normal direction, implying that the area moves relatively upward. In this area, on average a maximum velocity in the normal direction of ∼8 mm/y is found. At the northeast, relative nor-

mal displacements are near-zero but significant transversal displacements are estimated. Northeast of the fault, we find positive transversal displacements, while at the southwest of the fault, transversal displacements are negative, meaning that the two sides of the fault move away from each other, i.e., there is extensional strain. The blue band just northeast of the fault shows the largest horizontal displacements, up to ∼6 mm/y. Since the displacement time-series has a length of almost four years, the total displacement is ∼2.3 cm. As the area with the largest transversal displacements has a width of ∼400 m, this results in ∼23 $\mu\varepsilon$ (micro-strain).

Comparing the strapdown with the neglect-north results, we find significant differences. While the results are strongly dependent on the hypothesis that surface movement is correlated with the fault and its orientation—an assumption that can be disputed—we prefer the inclusion of such contextual information over a 'blind' approach with a decomposition in the arbitrary east-up plane. In general, adding extra information to the estimation problem will lead to better interpretable displacement estimates, since (i) we obtain 3D instead of 2D displacement vectors, (ii) we include the horizontal and vertical confidence regions (see Fig. 11 e and f), and (iii) we avoid the inherent bias introduced by the neglect-north approach. The approach requires an explicit statement on the contextual information that is used.

5 Merits and limitations

The strapdown method lies halfway in the spectrum between 'geometry-only' methods, which are purely based on the geometry of the observations, agnostic of the expected displacement phenomena, and 'advanced physical' methods, which assume knowledge of the physics of the driving mechanisms and can produce forward or inverse models related to the physical parameters. The strapdown method is based on the assumption that in many cases we can do better than the geometry-only methods, by making pragmatic use of non-disputed contextual knowledge on the problem at hand. It makes sense not to disregard this contextual information, as long as it is explicitly stated and refutable. Likewise, in terms of limitations, the strapdown method cannot replace a thorough combination of physical information on a particular case study with geometric displacements estimated from InSAR. Inclusion of prior expert knowledge to the estimation problem should always result in a more optimal result. For example, when forward models are available, it may not even be needed to perform a decomposition of the viewing geometries, since it is easy to evaluate the model in the LoS viewing geometry directly. Yet, such a model of the driving mechanisms may not be always available. The conventional east-up decomposition, i.e., a geometry-only method, yields biased results, particularly in the up direction, and it is in fact a 'neglect-north' approach. There is no physical reason why horizontal displacements in, e.g., the east direction are more common than in the north direction. Applying the unbiased strapdown method requires the orientation of the local TLN reference system at all locations, which comes with uncertainty. Yet, since this uncertainty is expressed and used in the estimation, the resulting displacement vector orientation and magnitude have realistic confidence regions, which mitigates the likelihood of misinterpretation. The strapdown method is dependent on the existence of presumed Regions of Uniform Motion (RUMs), which is essentially an assumption, similar to the geometry-only and advanced physical methods, and the datasets from different viewing geometries need to find a common reference point.

6 Conclusions

The strapdown method makes it possible to estimate three-dimensional displacements from two satellite imaging geometries for deformation phenomena where the deformation mechanism is known to some extent, using minimal and largely undisputed contextual information. The method uses a location-dependent local reference system, with displacement occurring only in the transversal-normal plane, confined by a RUM. Since the orientation of the local frame is based on the physics of the problem at hand, the strapdown approach gives physically more relevant estimates compared to conventional geometry-only approaches, which are intrinsically biased, while not claiming optimality in the domain of advanced physical models. By quantifying the uncertainty in the knowledge about the orientation of the local frame, proper error propagation enables assessing the quality of the final estimates. In this way, even when the frame orientation is poorly known, it is still possible to estimate transversal and normal displacement components, and subsequently the east and north components, as long as the 'true' frame orientation is within the estimated orientation uncertainty. The method is practical, effective, unbiased, and largely generic, and can be characterized as "2D-local/3D-global".

Cartographic representations of the three-dimensional results include the re-introduction of classic geodetic vector-based visualizations, including confidence ellipses, which enables a more profound interpretation of the results.

A The projector $P^R_{\mathrm{LoS}^\perp}$

Equation (2) contains $P^R_{\mathrm{LoS}^\perp}$, the projector that projects the displacement vector d_{TLN} onto the LoS along a plane orthogonal to the LoS. $P^R_{\mathrm{LoS}^\perp}$ is a function of Λ, Ω, and Φ with size

3×1, i.e., $P^R_{\text{LoS}^\perp} = [P_T, P_L, P_N]$, with

$$\begin{aligned} P_T =& \big(\sin\theta \sin\alpha_d \cos\Lambda - \sin\theta \cos\alpha_d \sin\Lambda\big) \cos\Omega \\ & - \big(-(\sin\theta \sin\alpha_d \sin\Lambda + \sin\theta \cos\alpha_d \cos\Lambda) \sin\Phi \\ & + \cos\theta \cos\Phi\big) \sin\Omega \\ P_L =& \big(\sin\theta \sin\alpha_d \sin\Lambda + \sin\theta \cos\alpha_d \cos\Lambda\big) \cos\Phi \\ & + \cos\theta \sin\Phi \\ P_N =& \big(\sin\theta_m \sin\alpha_d \cos\Lambda - \sin\theta \cos\alpha_d \sin\Lambda\big) \sin\Omega \\ & + \big(-(\sin\theta_m \sin\alpha_d \sin\Lambda + \sin\theta \cos\alpha_d \cos\Lambda) \sin\Phi \\ & + \cos\theta \cos\Phi\big) \cos\Omega. \end{aligned} \tag{14}$$

Acknowledgements We would like to thank Dr. Jolivet, Dr. Grandin, and an anonymous reviewer for the valuable comments and suggestions. We acknowledge SkyGeo for support and providing the data for the two case studies. This work is part of the project of the research programme DeepNL (NWO DEEP.NL.2018.052) which is financed by the Dutch Research Council (NWO).

References

Bechor NB, Zebker HA (2006) Measuring two-dimensional movements using a single insar pair. Geophys Res Lett. https://doi.org/10.1029/2006GL026883

Brinkman J (2016) Invloed van bodemdaling door zoutwinning Nedmag op bebouwing. Deltares report

Brouwer WS, Hanssen RF (2023) A treatise on InSAR geometry and 3-D displacement estimation. IEEE Trans Geosci Remote Sens 61:1–11

Caro Cuenca M, Hooper AJ, Hanssen RF (2013) Surface deformation induced by water influx in the abandoned coal mines in Limburg, The Netherlands observed by satellite radar interferometry. J Appl Geophys 88:1–11

Cascini L, Fornaro G, Peduto D (2010) Advanced low-and full-resolution dinsar map generation for slow-moving landslide analysis at different scales. Eng Geol 112(1–4):29–42

Cavalié O, Jónsson S (2014) Block-like plate movements in eastern Anatolia observed by InSAR. Geophys Res Lett 41(1):26–31

Chang L, Dollevoet R, Hanssen R (2014) Railway infrastructure monitoring using satellite radar data. Int. J. Railw. Technol 3:79–91

Chang L, Dollevoet RP, Hanssen RF (2018) Monitoring line-infrastructure with multisensor sar interferometry: products and performance assessment metrics. IEEE J Sel Topics Appl Earth Observ Remote Sens 11(5):1593–1605

Colesanti C, Wasowski J (2006) Investigating landslides with space-borne synthetic aperture radar (SAR) interferometry. Eng Geol 88(3–4):173–199

Crosetto M, Solari L, Mróz M, Balasis-Levinsen J, Casagli N, Frei M, Oyen A, Moldestad DA, Bateson L, Guerrieri L et al (2020) The evolution of wide-area DInSAR: from regional and national services to the European ground motion service. Remote Sens 12(12):2043

Dzurisin D, Lisowski M (2007) Analytical volcano deformation source models. Geodetic monitoring techniques, Volcano deformation, pp 279–304

Fialko Y, Sandwell D, Agnew D, Simons M, Shearer P, Minster B (2002) Deformation on nearby faults induced by the 1999 Hector Mine earthquake. Science 297:1858–1862

Ford AL, Forster RR, Bruhn RL (2003) Ice surface velocity patterns on Seward Glacier, Alaska/Yukon, and their implications for regional tectonics in the Saint Elias Mountains. Ann Glaciol 36:21–28

Fowler CMR (1990) The solid earth: an introduction to global geophysics. Cambridge University Press, Cambridge

Geertsma J (1973) A basic theory of subsidence due to reservoir compaction: the homogeneous case. Verhandelingen van het Koninklijk Nederlands geologisch mijnbouwkundig Genootschap 28:43–62

Gray AL, Mattar KE, Vachon PW (1998) InSAR results from the RADARSAT Antarctic mapping mission data: estimation of data using a simple registration procedure. In International Geoscience and Remote Sensing Symposium, Seattle, Washington, USA, 6–10 July 1998, pages 1638–1640

Greif V, Vlcko J (2012) Monitoring of post-failure landslide deformation by the PS-InSAR technique at Lubietova in Central Slovakia. Environ Earth Sci 66(6):1585–1595

Hanssen RF (2001) Radar interferometry: data interpretation and error analysis, volume 2. Springer Science & Business Media

Heitfeld M, Klunker J e. a (2016) Na-ijlende gevolgen steenkolenwinning Zuid-Limburg - Summary report with integrated Bow-Tie-Analysis, volume 1. Projectgroep GS-SL

Joughin IR, Kwok R, Fahnestock MA (1998) Interferometric estimation of three-dimensional ice-flow using ascending and descending passes. IEEE Trans Geosci Remote Sens 36(1):25–37

Kratzsch H (1983) Mining subsidence engineering. Springer Science & Business Media

Massonnet D, Feigl KL (1998) Radar interferometry and its application to changes in the earth's surface. Rev Geophys 36(4):441–500

Mattar KE, Vachon PW, Geudtner D, Gray AL, Cumming IG, Brugman M (1998) Validation of Alpine glacier velocity measurements using ERS tandem-mission SAR data. IEEE Trans Geosci Remote Sens 36(3):974–984

Mohr JJ (1997) Repeat Track SAR Interferometry. An investigation of its Utility for Studies of Glacier Dynamics. PhD thesis, Technical University of Denmark, Copenhagen

Mohr JJ, Reeh N, Madsen SN (1998) Three-dimensional glacial flow and surface elevation measured with radar interferometry. Nature 291:273–276

Müller D, Preusse A (2018) Use of the area of main influence to fix a relevant boundary for mining damages in Germany. Int J Min Sci Technol 28(1):79–83

Notti D, Herrera G, Bianchini S, Meisina C, García-Davalillo JC, Zucca F (2014) A methodology for improving landslide PSI data analysis. Int J Remote Sens 35(6):2186–2214

Özer IE, van Leijen FJ, Jonkman SN, Hanssen RF (2019) Applicability of satellite radar imaging to monitor the conditions of levees. J Flood Risk Manag 12(S2):e12509

Pöttgens J (1985) Uplift as a result of rising mine waters. In The Development Science and Art of Mineral Surveying, Proceedings of the 6th International Congress. International Society for Mine Surveying, Harrogate UK, volume 2

Rocca F et al (2003) 3D motion recovery with multi-angle and/or left right interferometry. In Proceedings of the third International Workshop on ERS SAR

Scheiber R, Moreira A (2000) Coregistration of interferometric SAR images using spectral diversity. IEEE Trans Geosci Remote Sens 38(5):2179–2191

Strozzi T, Luckman A, Murray T, Wegmuller U, Werner C (2002) Glacier motion estimation using sar offset-tracking procedures. IEEE Trans Geosci Remote Sens 40(11):2384–2391

Titterton D, Weston JL, Weston J (2004) Strapdown inertial navigation technology, volume 17. IET

Van Balen R, Kasse C, Wallinga J, Woolderink H (2021) Middle to late pleistocene faulting history of the heerlerheide fault, roer valley rift system, influenced by glacio-isostasy and mining-induced displacement. Quatern Sci Rev 268:107111

Van Bergen F, Pagnier H, Van Tongeren P (2007) Peat, coal and coalbed methane. Geology of the Netherlands. Royal Netherlands Academy of Arts and Sciences, pages 265–282

van Leijen FJ (2014) Persistent Scatterer Interferometry based on Geodetic Estimation Theory. Number 86 in Publications on Geodesy. NCG. 195 pp

Van Natijne A, Bogaard T, van Leijen F, Hanssen R, Lindenbergh R (2022) World-wide InSAR sensitivity index for landslide deformation tracking. Int J Appl Earth Obs Geoinf 111:102829

Wright TJ, Parsons BE, Lu Z (2004) Toward mapping surface deformation in three dimensions using insar. Geophys Res Lett. https://doi.org/10.1029/2003GL018827

Wright TJ, Parsons BE, Lu Z (2004) Towards mapping surface deformation in three dimensions using InSAR. Geophys Res Lett. https://doi.org/10.1029/2003GL018827

Yu B, Liu G, Zhang R, Jia H, Li T, Wang X, Dai K, Ma D (2013) Monitoring subsidence rates along road network by persistent scatterer SAR interferometry with high-resolution TerraSAR-X imagery. J Modern Transp 21:236–246